Oscillating Hydrogen Bubbles at Pt Microelectrodes

Aleksandr Bashkatov,[1,*] Syed Sahil Hossain,[1] Xuegeng Yang,[1] Gerd Mutschke,[1] and Kerstin Eckert[1,2,†]

[1]*Institute of Fluid Dynamics, Helmholtz-Zentrum Dresden-Rossendorf, Bautzner Landstrasse 400, Dresden, 01328 Germany*

[2]*Institute of Process Engineering and Environmental Technology, Technische Universität Dresden, Dresden, 01062 Germany*

(Received 16 April 2019; revised manuscript received 12 July 2019; published 19 November 2019)

The dynamics of hydrogen bubbles produced via electrolysis in acidic electrolytes is studied in a combination of experiments and numerical simulations. A transition from monotonic to oscillatory bubble growth is observed after $2/3$ of the bubble lifetime, if the electric potential exceeds -3 V. This work analyzes characteristic features of the oscillations in terms of bubble geometry, the thickness of the microbubble carpet, and the oscillation frequency. An explanation of the oscillation mechanisms is provided by the competition between buoyancy and electric force, the magnitude of which depends on the carpet thickness. Both the critical carpet thickness at detachment and the oscillation frequencies of the bubble as predicted by the model agree well with the experiment.

DOI: 10.1103/PhysRevLett.123.214503

The growth of gas bubbles is a ubiquitous phenomenon in nature and engineering [1]. Impressive examples are related to sonoluminescence [2,3] or cavitation phenomena [4–6] or even the evolution of CO_2 bubbles in champagne [7]. The growth of hydrogen bubbles in light-driven water splitting [8–10] or water electrolyzers is a particularly interesting problem of high practical relevance due to the prominent role of hydrogen in energy storage via power-to-gas processes [11–14]. Alkaline water electrolysis is still the most mature and least platinum-consuming technology, albeit one suffering from inadequate efficiency. The latter can be increased by reducing the Ohmic losses [15–19] arising from the reduction of conductivity and the deactivation of the electrode by the nonconducting bubbles. If the hydrogen bubbles are to be transported away from the electrodes faster, this inherently requires a better understanding of bubble growth and detachment.

Tremendous efforts to resolve the growth dynamics of hydrogen bubbles during the past five decades have brought evidence on the growth law for the bubble radius $R_b \propto t^x$, where the exponent is equal to $1/2$ if the growth is controlled by the bulk diffusion of dissolved hydrogen and equal to $1/3$ if the hydrogen injection occurs at the foot of the bubble and mostly by coalescence with smaller bubbles [20,21]. By contrast, the current understanding of the force balance [19,22–24] does not cover the variety of existing observations. Among the unresolved phenomena, one of the most prominent is the sudden jump off of bubbles from the electrode, and their subsequent reattachment [25–27]. There has been speculation as to whether electrostatic attraction, the solutal Marangoni effect [16], or coalescence, as recently proposed in [27], is behind the physics of the reattachment. While the solutal Marangoni effect due to the concentration dependence of surface tension can be ruled out based on recent works [28,29], the role of electrostatic interactions and coalescence remains unclear.

To unravel the physics behind the oscillatory phenomena in water electrolysis, the present Letter combines experiments and numerical simulations at a microelectrode. This is the method of choice [21,30,31] to study single H_2 bubbles at high spatial resolution, since microelectrodes provide a low number of nucleation sites and enable relatively large bubbles to be grown. In model experiments [cf. Fig. 1(a)] the features of long-lasting oscillations of hydrogen bubbles are studied. By means of theoretical analysis, the role of the electrical force during these bubble oscillations is clarified.

In the experiments, single H_2 bubbles are generated on a horizontally installed $\varnothing 100\ \mu$m Pt microelectrode, see Fig. 1(a), using a three-electrode setup. A mercury-mercurous sulfate electrode (MSE, 0.65 V vs SHE) and a Pt wire ($\varnothing$1 mm) served as the reference electrode and anode, respectively [21]. Electrolysis was carried out in an acidic electrolyte (0.5 $\mathrm{mol\,dm^{-3}}$ and 1 $\mathrm{mol\,dm^{-3}}$ H_2SO_4) in potentiostatic mode in the potential range between -2 and -7 V for 30 s. To analyze the bubble evolution, high-speed microscopic shadowgraphy using a camera (IDT NX4-S1) connected to the microscope was applied at 1000 frames per second and a spatial resolution of up to 820 pix/mm, coupled

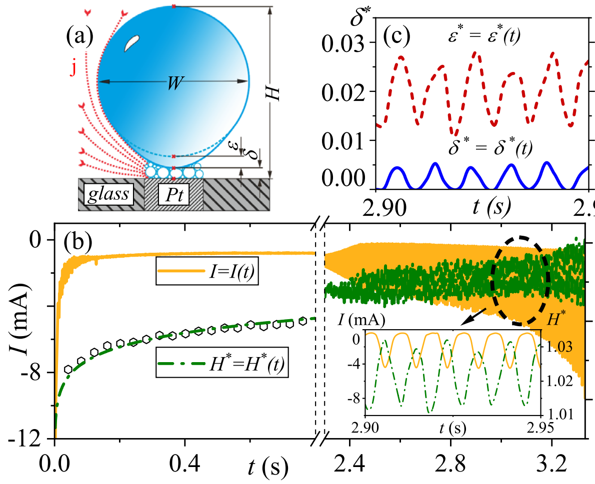

FIG. 1. (a) Scheme of the slightly deformed spherical bubble, sitting on the Pt electrode, and the carpet of microbubbles beneath, with their relevant geometric parameters. (b) Electric current I (solid line) and aspect ratio H^* (open circles: experiment; dash-dotted line: fit) of the bubbles versus time in 1 mol dm^{-3} H_2SO_4 at −5 V. The inset enlarges the oscillations of I and H^* in the dashed oval region. (c) Corresponding oscillations of the carpet thickness δ^* (solid line) and the bubble elongation ε^* (dashed line).

to electric current measurements with a sampling rate of 1 kHz (see the Supplemental Material [32]).

The bubble growth at the microelectrode takes place via coalescence with small bubbles, forming a microbubble carpet at the cathode, which is analyzed later on. The geometric parameters of the bubble during its evolution [Fig. 1(a)] were extracted by image processing of the shadowgraphs based on the Canny edge detection method in Matlab R2016a (see the Supplemental Material [32]): the height H of the bubble apex above the electrode, the bubble width W, the thickness δ of the carpet of microbubbles and the elongation of the bubble foot, ε. Careful inspection of $W(t)$ has shown that fluctuations of the bubble width are negligible. Hence, W is used to obtain nondimensional quantities, marked by a star *, from the measured ones, e.g., $H/W = H^*$.

In Figs. 1(b)–1(c), these quantities are plotted, together with the electric current, as a function of time over the entire life cycle of the bubble for 1 mol dm^{-3} H_2SO_4 at −5 V. During the first two thirds of its evolution, the bubble follows the conventional path at the microelectrodes, characterized by the growth law, $R \propto t^{1/3}$, in accordance with, e.g., [21,41,42]. However, during the last third, the bubble evolution switches into a completely different, *oscillatory* mode. The inset shows that the maxima of H^* and $|I|$ coincide: if the bubble moves upward (H^* increases) the contact area between the bubble and the cathode is reduced and the current $|I|$ grows. However, there is no direct bubble-electrode contact. This is due to the fact that the bubble oscillations are accompanied by the formation of a carpet of small (micro)bubbles beneath the mother bubble, cf. Figs. 1(a) and 2(c).

In the carpet, which has a thickness of $\delta(t)$, continuous nucleation, growth, and coalescence with the mother bubble takes place. The carpet acts like a cushion between the electrode and the bubble, and determines the growth of the mother bubble. Surprisingly, $H^* \neq 1 + \delta^*$ where $\delta^* = \delta/W$. The resulting residuum needs to be assigned to a third contribution, ε. It results from the elongation of the bubble foot [cf. Fig. 1(a)], mainly caused by buoyancy, as $\varepsilon^* = \varepsilon/W = H^* - \delta^* - 1$. The evolution of ε^* and δ^* is shown in the Fig. 1(c). Both quantities are oscillating in phase, whereby the oscillation amplitude of ε^* is about three times larger than the one of δ^*. Besides, ε^* clearly shows a mean offset of about 0.02.

Figure 2(a) presents the carpet thickness δ for several potentials over the entire bubble life time. Marked by way of example at the −4 V curve, three characteristic times can be identified: the first appearance of the carpet at t_1, the start of the oscillations at t_2, and finally the detachment of the mother bubble at t_3, the latter being defined by the highest peak of δ oscillations. The corresponding carpet thicknesses δ_i are indicated in parallel. Figure 2(b) enlarges the δ and I oscillations versus time at −7 V. It shows that the peaks coincide, which might already be expected from Fig. 1. At the lowest potential, −2 V, see the far left curve in Fig. 2(a), the carpet with a barely measurable thickness of $\delta_1 \sim 1.2$ μm is already present at the moment when the mother bubble is formed, thus $t_1 \approx 0$. The carpet thickness grows monotonically with a relatively steep increase before detachment for both −2 and −3 V. As the potential increases, the appearance of the microbubble carpet at t_1 is shifted towards later stages of the bubble evolution.

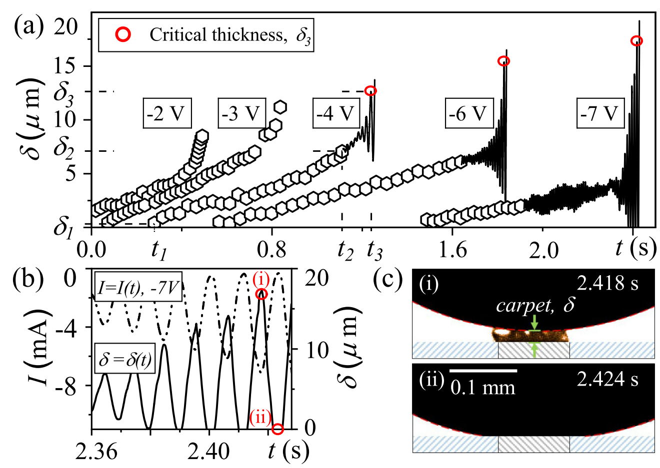

FIG. 2. (a) Measured carpet thickness δ versus time in 0.5 mol m^{-3} H_2SO_4 for different potentials. Characteristic times t_i and thicknesses δ_i are indicated (see text). (b) Correlation between δ and the corresponding current response at -7 V. (c) Two snapshots of the carpet thickness at the stages (i) and (ii) indicated in (b).

For the higher potentials, −4, −6, and −7 V, the monotonic growth of δ is replaced at t_2 by an oscillatory growth (occurring simultaneously with the I and H^* oscillations), which lasts until detachment. Two opposing trends are followed by δ_2 and δ_3: while δ_2 decreases with increasing potential, i.e., the oscillations already occur at smaller carpet thickness, the critical carpet thickness at which detachment takes place, δ_3, increases. Generally, the higher the potential, the higher the growth rate of the mother bubble. Since its growth is entirely controlled by the coalescence rate of the microbubbles, a larger potential also implies a faster microbubble production rate. As a result, both the buoyancy of the mother bubble and the number of larger microbubbles in the carpet increase, raising the carpet thickness.

Figure 2(c) visualizes the carpet at two distinct stages (i) and (ii) of the oscillation as marked in red in Fig. 2(b). Stage (i) represents the bubble at its maximum position, and stage (ii) marks the minimum position within the oscillation period, at which the microbubble carpet is nicely visible.

When the impact of coalescence between mother bubble and gas layer is neglected, the mother bubble with a radius R, sitting on the gas carpet, experiences primarily three forces prior to detachment: (i) buoyancy given by $F_b = \frac{4}{3}\pi R^3 \Delta\rho g$, where $\Delta\rho = \rho_l - \rho_g$ refers to the density difference between gas and electrolyte; (ii) the force F_e exerted by the electric field on the charge adsorbed at bubble interface; and (iii) the hydrodynamic force F_M caused by the thermocapillary Marangoni flow. As the H_2 bubble is insulating, the electric field ($\vec{E}$) is tangential to the interface. If we assume that the interface has a uniform surface charge density of σ, the electric force is given by $\vec{F}_e = \sigma \int \vec{E} dA$ where the integration is carried out over the entire interface. Decomposing the interfacial electric field into horizontal and vertical components, i.e., $\vec{E} = E_x\hat{x} + E_y\hat{y}$ [cf. the coordinate system displayed in Fig. 3(a)], it can be shown that the net electric force in vertical (y) direction is

$$F_{e,y} = \sigma \int E_y dA \tag{1}$$

since $\int E_x dA = 0$ due to rotational symmetry. For simplicity we will refer to $F_{e,y}$ as F_e henceforth.

It was reported in [29] that a thermocapillary Marangoni flow exists at electrogenerated bubble interfaces on microelectrodes. Hence the bubble experiences Marangoni force given by the integration of thermocapillary stress over the interface [29],

$$F_M = -\int \tau_M dA \tag{2}$$

where $\tau_M = (\partial\gamma/\partial T)(\partial T/\partial s)$ is due to the variation of interfacial tension γ with temperature T along a length s at the interface.

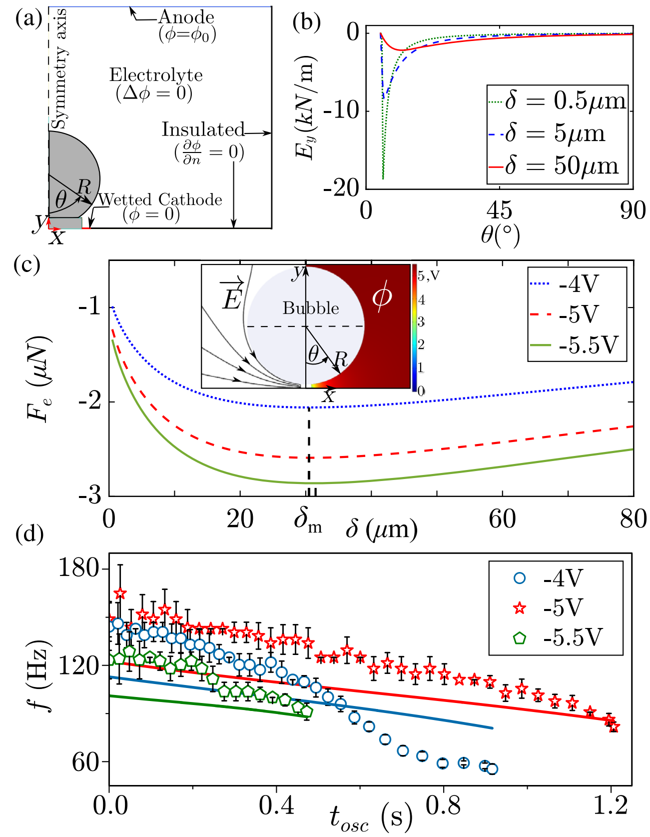

FIG. 3. (a) Computational domain (not to scale). (b) E_y distribution over the interface for −4 V. (c) Dependence of the electric force F_e on the thickness δ of the bubble carpet. Force minima marked by vertical dashed line. Inset: potential (ϕ) and electric field ($\vec{E}$) distribution near the bubble. (d) Oscillation frequency of the bubble versus time. Symbols and lines refer to measurement and model estimation, respectively. The error bars correspond to the standard deviation calculated from a group of eight bubbles observed in one experiment (1 mol dm^{-3} H_2SO_4 solution).

To obtain a quantitative estimate of F_e, we solve for the electric potential distribution in the cell $\Delta\phi = 0$, using FEM simulations in COMSOL 5.4 with Dirichlet boundary conditions at the electrodes and all other boundaries being insulating. The computation domain is shown in Fig. 3(a). The electrically insulating microbubble carpet covers the cathode so that 24% of the electrode area in the outer region is wetted by electrolyte (cf. Fig. 7 in [21]). The mother bubble is assumed to be spherical in shape with a diameter taken as the experimentally measured departure diameter.

To calculate F_e, an estimate for σ is required. As the solution pH is below the isoelectric point, the hydrogen-water interface is expected to be positively charged [43] due to the specific adsorption of protons at the interface and therefore F_e acts downward ($-y$ direction). It was shown in [29] that also the Marangoni force experienced by the bubble acts against buoyancy. Therefore, at the moment of detachment, the force equilibrium at the bubble is given by

$F_e + F_M = F_b$. Thus combining this with Eq. (1), the surface charge density can be estimated as $\sigma = (F_b - F_M)/f_e$, where $f_e = \int E_y dA$.

Hence, F_M is required to be calculated to estimate σ. Therefore we solve for the temperature and flow distribution in the cell for the domain shown in Fig. 3(a) by the methodology described in [29]. As the Pt electrode carries significant heat away from the fluid, the counter and working electrodes as well as the surrounding glass cuvette were included in the computation domain.

As the carpet thickness at detachment is known for $0.5\ \mathrm{mol\,dm^{-3}}$ H_2SO_4 solution from experiment, we obtain the estimate of σ for different electrode potential in $10^{-3}\ \mathrm{C/m^2}$ as 1.94 (−4 V), 2.20 (−6 V), and 1.81 (−7 V). Obviously, σ does not vary considerably with the electrode potential and, therefore, we take the average value $\sigma = (1.98 \pm 0.19) \times 10^{-3}\ \mathrm{C/m^2}$ as an estimate of the surface charge density. We further assume in the following that a quasiconstant thermocapillary Marangoni force exists during the fast bubble oscillations ($f \sim 100$ Hz). As the temperature at the interface is determined by convection (Pe $\gg 1$) [29], this approximation is justified by the separation of the timescales of oscillation ($2/f \sim 5$ ms) and Marangoni convection [$R/|\vec{u}| \sim 0.5\ \mathrm{mm}/(10\ \mathrm{mm/s}) = 50$ ms]. Hence, the electric force remains as the primary driving force for the oscillations.

As σ is assumed to be uniform, F_e is determined by the integral of E_y over the interface. The interfacial distribution of E_y for different carpet thicknesses is shown in Fig. 3(b). As the field lines are directed downwards [see inset of Fig. 3(c)], E_y is negative over the interface. $|E_y|$ increases sharply at small polar angle θ [see Fig. 3(b)] and gradually decreases to zero as θ increases. This can also be visualized from the ϕ distribution shown in the inset of Fig. 3(c). With increasing δ, the peak in the E_y distribution decreases. As a result, a more uniform field distribution over the entire interface is established. This $E_y(\theta)$ behavior results in a variation of F_e with δ, i.e., $F_e(\delta) = 2\pi\sigma R^2 \int_0^{\pi} E_y(\theta;\delta)\sin\theta d\theta$, where $dA = 2\pi R^2 \sin\theta d\theta$ is substituted in Eq. (1).

$F_e(\delta)$ for different electrode potentials is shown in Fig. 3(c). As $\sigma > 0$ and $E_y \le 0$, $F_e < 0$; i.e., it acts against buoyancy as already mentioned before. $|F_e|$ increases with increasing δ until it attains a maximum at δ_m and reduces afterwards. This position-dependent electric force acts like a spring causing the bubble to oscillate. As F_b increases due to continual bubble growth, the oscillation amplitude increases till δ_m. Beyond δ_m, any further increment in oscillation amplitude causes a reduction in $|F_e|$, which can no longer counteract F_b, hence resulting in bubble detachment. Thus our model predicts that $\delta_m \sim 30\ \mu$m, shown by vertical dashed line in Fig. 3(c), is the final carpet thickness at the instant of detachment. This correlates well with experimental observation of δ_3 (10 μm, …, 20 μm) shown in Fig. 2.

As the position dependence of the electric force is responsible for the oscillatory behavior observed, we approximate this restoring force by a linear spring ($F_e \approx -k\delta$) and estimate the oscillation frequency as,

$$f = \frac{1}{2\pi}\sqrt{\frac{k}{m}} \tag{3}$$

The spring constant k is approximated as the slope of the chord of $F_e(\delta)$, $\Delta F_e/\Delta\delta$ between 0.5 μm and 15 μm, see Fig. 3(c). The oscillation mass is given by $m = m_{\mathrm{bubble}} + m_{\mathrm{added}}$, where m_{bubble} is the mass of the bubble itself and m_{added} is the added inertia as the bubble motion displaces adjacent liquid. For a sphere, added inertia is the mass of displaced volume halved [44], i.e., $m_{\mathrm{added}} = \frac{2}{3}\pi R^3 \rho$. As the density of hydrogen is much lower than that of the electrolyte solution, $m_{\mathrm{bubble}} \ll m_{\mathrm{added}}$ and hence $m \approx m_{\mathrm{added}}$. Furthermore, as the bubble clearly continues to grow during the oscillatory regime (cf. Fig. 1), the temporal evolution of the bubble radius observed experimentally for a $1\ \mathrm{mol\,dm^{-3}}$ H_2SO_4 electrolyte is considered when calculating the frequency.

Figure 3(d) shows that the resulting oscillation frequency decreases with time, as also observed in experiments. In the experiments it is also observed that the oscillation frequency increases when the potential difference is increased from −4 to −5 V, but drops again upon a further increment to −5.5 V. This phenomenon is correctly predicted by the spring-mass model [cf. Fig. 3(d)] and can be explained by Eq. (3). The $F_e(\delta)$ curves seen in Fig. 3(c) grow steeper when the potential is increased, and the bubble also grows in size as the applied potential difference is increased. Thus both k and m increase along with the cell voltage. These two competing effects result in the reversal in the trend observed in Fig. 3(d).

Next, we comment on the interfacial charge density σ, which is an important parameter in interfacial electrokinetics. From measurements [45,46], it is known that the zeta potential quickly plateaus below the isoelectric point (IEP). Hence it can be assumed that the interface of our bubble in a 0.5 or $1\ \mathrm{mol\,dm^{-3}}$ H_2SO_4 solution (pH < IEP) possesses electrical properties comparable to Refs. [45,46] at a low pH. Taking the interface potential to be the same as the zeta potential and using the Grahame equation [47], the interfacial charge density can be calculated at low pHs as $1.55 \times 10^{-3}\ \mathrm{C/m^2}$ [45] and $6.99 \times 10^{-3}\ \mathrm{C/m^2}$ [46], respectively. Thus our estimate of $\sigma \approx 2 \times 10^{-3}\ \mathrm{C/m^2}$ from the force equilibrium at the bubble is in good agreement with experimentally measured zeta potentials and for the first time establishes an estimate of the surface charge density of gas interfaces in highly acidic solutions.

This finding remains robust when bubble deformations are acknowledged. By comparing the numerical results of $\varepsilon^* = 0$ and $\varepsilon^* = 0.02$ shown in Fig. 1, the assumption of bubble sphericity results in an overprediction of σ by approximately 40%, thus still maintaining the correlation with the other experimental observations. This deviation vanishes when predicting f as k is the slope of $F_e(\delta)$, the product of σ and f_e.

Finally, we remark that the electric force F_e can be interpreted as originating from electrocapillarity as demonstrated in the Supplemental Material [32]. Hence, both restoring forces have their nature in different facettes of capillarity. A refined quantification of these Marangoni force variations will help to improve the present model.

To conclude, two new insights into the growth of hydrogen bubbles during water electrolysis at microelectrodes have been established: the transition toward oscillatory growth and the permanent existence of a carpet of microbubbles below a hydrogen bubble. A conclusive explanation of the oscillation mechanism has been provided in the form of a competition between buoyancy and the electric force. The electric force reaches a maximum at a carpet thickness of about 30 μm, which corresponds well with the carpet thickness at which the bubble detaches in the experiment. Up to that carpet thickness, the electric force is able to pull the bubble back to the electrode, sustaining the oscillations.

The issues which remain unsolved include the extent to which coalescence between the bubble and the bubble carpet, which may also force a detached bubble to return to the electrode, contributes to the observed oscillations.

This project is supported by the German Space Agency (DLR) with funds provided by the Federal Ministry of Economics and Technology (BMWi) due to an enactment of the German Bundestag under Grant No. DLR 50WM1758 (project MADAGAS). A. B. conducted the experiments and identified the phenomena, S. S. H. did analytical modeling and performed simulations, X. Y., G. M., and K. E. conceptualized the study.

*Corresponding author.
a.bashkatov@hzdr.de
†Corresponding author.
k.eckert@hzdr.de

[1] D. Lohse, Bubble puzzles: From fundamentals to applications, Phys. Rev. Fluids **3**, 110504 (2018).
[2] M. P. Brenner, S. Hilgenfeldt, and D. Lohse, Single-bubble sonoluminescence, Rev. Mod. Phys. **74**, 425 (2002).
[3] K. S. Suslick and D. J. Flannigan, Inside a collapsing bubble: sonoluminescence and the conditions during cavitation, Annu. Rev. Phys. Chem. **59**, 659 (2008).
[4] C. E. Brennen, *Cavitation and Bubble Dynamics* (Cambridge University Press, Cambridge, England, 2014).
[5] D. Obreschkow, P. Kobel, N. Dorsaz, A. de Bosset, C. Nicollier, and M. Farhat, Cavitation Bubble Dynamics Inside Liquid Drops in Microgravity, Phys. Rev. Lett. **97**, 094502 (2006).
[6] E. Zwaan, S. Le Gac, K. Tsuji, and C.-D. Ohl, Controlled Cavitation in Microfluidic Systems, Phys. Rev. Lett. **98**, 254501 (2007).
[7] G. Liger-Belair, G. Polidori, and P. Jeandet, Recent advances in the science of champagne bubbles, Chem. Soc. Rev. **37**, 2490 (2008).
[8] Z. Wang, C. Li, and K. Domen, Recent developments in heterogeneous photocatalysts for solar-driven overall water splitting, Chem. Soc. Rev. **48**, 2109 (2019).
[9] T. Takata and K. Domen, Particulate photocatalysts for water splitting: recent advances and future prospects, ACS Energy Lett. **4**, 542 (2019).
[10] K. Brinkert, M. H. Richter, Ö. Akay, J. Liedtke, M. Giersig, K. T. Fountaine, and H.-J. Lewerenz, Efficient solar hydrogen generation in microgravity environment, Nat. Commun. **9**, 2527 (2018).
[11] M. Götz, J. Lefebvre, F. Mörs, A. M. Koch, F. Graf, S. Bajohr, R. Reimert, and T. Kolb, Renewable power-to-gas: a technological and economic review, Renewable Energy **85**, 1371 (2016).
[12] S. Chu, Y. Cui, and N. Liu, The path towards sustainable energy, Nat. Mater. **16**, 16 (2017).
[13] V. R. Stamenkovic, D. Strmcnik, P. P. Lopes, and N. M. Markovic, Energy and fuels from electrochemical interfaces, Nat. Mater. **16**, 57 (2017).
[14] X. Zhao, H. Ren, and L. Luo, Gas Bubbles in Electrochemical Gas Evolution Reactions, Langmuir **35**, 5392 (2019).
[15] J. Eigeldinger and H. Vogt, The bubble coverage of gas-evolving electrodes in a flowing electrolyte, Electrochim. Acta **45**, 4449 (2000).
[16] S. Lubetkin, The motion of electrolytic gas bubbles near electrodes, Electrochim. Acta **48**, 357 (2002).
[17] H. Vogt and R. J. Balzer, The bubble coverage of gas-evolving electrodes in stagnant electrolytes, Electrochim. Acta **50**, 2073 (2005).
[18] K. Zeng and D. Zhang, Recent progress in alkaline water electrolysis for hydrogen production and applications, Prog. Energy Combust. Sci. **36**, 307 (2010).
[19] A. Taqieddin, M. R. Allshouse, and A. N. Alshawabkeh, Critical Review—Mathematical Formulations of Electrochemically Gas-Evolving Systems, J. Electrochem. Soc. **165**, E694 (2018).
[20] S. Lubetkin, The fundamentals of bubble evolution, Chem. Soc. Rev. **24**, 243 (1995).
[21] X. Yang, F. Karnbach, M. Uhlemann, S. Odenbach, and K. Eckert, Dynamics of single hydrogen bubbles at a platinum microelectrode, Langmuir **31**, 8184 (2015).
[22] L. Zeng, J. Klausner, D. Bernhard, and R. Mei, A unified model for the prediction of bubble detachment diameters in boiling systems—II. Flow boiling, Int. J. Heat Mass Transfer **36**, 2271 (1993).
[23] G. Duhar and C. Colin, Dynamics of bubble growth and detachment in a viscous shear flow, Phys. Fluids **18**, 077101 (2006).
[24] J. Chen, L. Guo, X. Hu, Z. Cao, and Y. Wang, Dynamics of single bubble departure from TiO_2 nanorod-array photoelectrode, Electrochim. Acta **274**, 57 (2018).
[25] D. E. Westerheide and J. Westwater, Isothermal growth of hydrogen bubbles during electrolysis, AIChE J. **7**, 357 (1961).

[26] P. J. Sides and C. W. Tobias, A close view of gas evolution from the back side of a transparent electrode, J. Electrochem. Soc. **132**, 583 (1985).

[27] S. M. H. Hashemi, P. Karnakov, P. Hadikhani, E. Chinello, S. Litvinov, C. Moser, P. Koumoutsakos, and D. Psaltis, A versatile and membrane-less electrochemical reactor for the electrolysis of water and brine, Energy Environ. Sci. **12**, 1592 (2019).

[28] X. Yang, D. Baczyzmalski, C. Cierpka, G. Mutschke, and K. Eckert, Marangoni convection at electrogenerated hydrogen bubbles, Phys. Chem. Chem. Phys. **20**, 11542 (2018).

[29] J. Massing, G. Mutschke, D. Baczyzmalski, S. S. Hossain, X. Yang, K. Eckert, and C. Cierpka, Thermocapillary convection during hydrogen evolution at microelectrodes, Electrochim. Acta **297**, 929 (2019).

[30] D. Fernandez, P. Maurer, M. Martine, J. Coey, and M. E. Mobius, Bubble formation at a gas-evolving microelectrode, Langmuir **30**, 13065 (2014).

[31] D. Baczyzmalski, F. Karnbach, X. Yang, G. Mutschke, M. Uhlemann, K. Eckert, and C. Cierpka, On the electrolyte convection around a hydrogen bubble evolving at a microelectrode under the influence of a magnetic field, J. Electrochem. Soc. **163**, E248 (2016).

[32] See Supplemental Material at http://link.aps.org/supplemental/10.1103/PhysRevLett.123.214503 for the description of appx. A—experimental setup, appx. B—image analysis, appx. C—electrocapillary effect, appx. D—comment on bubble radius evolution over time, which includes Refs. [21,30,33–40].

[33] V. G. Levich, *Physicochemical Hydrodynamics* (Prentice-Hall Inc., Englewood Cliffs, 1962).

[34] D. Johnson, *Electrocapillary Flows* (Springer, Berlin, Heidelberg, 2003).

[35] H.-J. Butt, K. Graf, and M. Kappl, *Physics and Chemistry of Interfaces* (Wiley-VCH Verlag, Weinheim, 2013).

[36] L. G. Leal, *Advanced Transport Phenomena: Fluid Mechanics and Convective Transport Processes* (Cambridge University Press, Cambridge, England, 2007), Vol. 7.

[37] J. Canny, in *Readings in Computer Vision* (Morgan Kaufmann, California, 1987), pp. 184–203.

[38] The MathWorks, Inc., “Edge detection,” https://www.mathworks.com/help/images/edge-detection.html, accessed: 2019-07-08.

[39] H. Verhaart, R. De Jonge, and S. Van Stralen, Growth rate of a gas bubble during electrolysis in supersaturated liquid, Int. J. Heat Mass Transfer **23**, 293 (1980).

[40] F. Karnbach, X. Yang, G. Mutschke, J. Fröhlich, J. Eckert, A. Gebert, K. Tschulik, K. Eckert, and M. Uhlemann, Interplay of the open circuit potential-relaxation and the dissolution behavior of a single H2 bubble generated at a Pt microelectrode, J. Phys. Chem. C **120**, 15137 (2016).

[41] R. Darby and M. Haque, The dynamics of electrolytic hydrogen bubble evolution, Chem. Eng. Sci. **28**, 1129 (1973).

[42] P. Kristof and M. Pritzker, Effect of electrolyte composition on the dynamics of hydrogen gas bubble evolution at copper microelectrodes, J. Appl. Electrochem. **27**, 255 (1997).

[43] N. Brandon, G. Kelsall, S. Levine, and A. Smith, Interfacial electrical properties of electrogenerated bubbles, J. Appl. Electrochem. **15**, 485 (1985).

[44] C. E. Brennen, *A Review of Added Mass and Fluid Inertial Forces*, Technical Report CR 82.010 (Naval Civil Engineering Laboratory, Port Hueneme, CA, USA, 1982).

[45] M. Takahashi, ζpotential of microbubbles in aqueous solutions: electrical properties of the gas- water interface, J. Phys. Chem. B **109**, 21858 (2005).

[46] P. Creux, J. Lachaise, A. Graciaa, J. K. Beattie, and A. M. Djerdjev, Strong specific hydroxide ion binding at the pristine oil/water and air/water interfaces, J. Phys. Chem. B **113**, 14146 (2009).

[47] J. N. Israelachvili, Intermolecular and surface forces, *Intermolecular and Surface Forces* (Academic Press, Boston, 2011).